ADVANCED FUNCTIONAL MATERIALS
www.afm-journal.de

Encoding Hidden Information onto Surfaces Using Polymerized Cholesteric Spherical Reflectors

*Yong Geng, Rijeesh Kizhakidathazhath, and Jan P. F. Lagerwall**

The omnidirectional Bragg reflection of cholesteric liquid crystals molded into spheres turns them into narrow-band retroreflectors with distinct circular polarization. It is shown that these cholesteric spherical reflectors (CSRs) can encode information onto surfaces for far-field optical read-out without false positives, as the selective retroreflectivity allows the background to be easily subtracted. In order to hide the encoding from detection by the human eye, the retroreflection band is tuned to the near-UV or IR spectra, allowing ubiquitous deployment of CSRs in human-populated environments. This opens diverse application opportunities, for instance, in supporting safe robotic navigation and in augmented reality. A key breakthrough is our ability to permanently embed CSRs in a binder such that undesired scattering and reflections are minimized. This is achieved by realizing CSRs as shells that are polymerized from the liquid crystalline state. The resulting shrinkage around an incompressible fluid deforms the thinnest region of each shell such that it ruptures at a well-defined point. This leaves a single small hole in every CSR that gives access to the interior, allowing complete embedding in the binder with optimized refractive index, minimizing visibility.

1. Introduction

Enormous societal gains have been suggested by bringing autonomous robots into human-populated environments, from reduced CO_2 emissions[1] and improved personal mobility[2] enabled by self-driving vehicles, to more efficient waste management[3] and resilient ecosystems[4] made possible by robot swarms. While such developments can be highly beneficial, many concerns may be raised, among the most important being related to safety: as demonstrated by recurring tragic fatalities, autonomous vehicles have an insufficient understanding of their environment despite state-of-the-art on-board sensor and computation technology.[5–9] In restricted environments like research labs or power plants, reliable localization and object identification by robots are ensured by labeling surfaces with *fiducial markers*,[10] patterns of black squares on white background similar to the well-known QR codes. Fiducial markers would be an enormous aid for robots deployed in human-populated spaces, but black-on-white grid patterns are aesthetically and architecturally disruptive. Out-of-lab operation also offers challenges from fast-moving, busy and dynamic environments, like in megacity centers. For fiducial markers to be useful in everyday environments, they must be rapidly and reliably detectable by robots, without false positives, yet humans should not notice them.

Here we propose a solution by replacing the black ink in traditional fiducial markers by cholesteric spherical reflectors (CSRs), spherical shells of polymerized cholesteric liquid crystal (CLC). They provide omnidirectional retroreflectivity that is polarization- and wavelength-selective,[11] and by tuning the operation band to the infrared (IR) or near-ultraviolet (near-UV, not harmful) spectra, the reflections are invisible to the human eye. We argue that robots, in contrast, would be able to detect the encoded information extremely efficiently and reliably using low-cost and simple machine vision equipment designed for the purpose, greatly improving their ability to make sense of, and safely navigate through, our natural human-populated environments.

Because CLCs are liquids, they can be processed in fluidic pathways into drops or shells[12] in which their unique chiral self-assembly ability results in the formation of a helically periodic structure that is spherically symmetric, provided that a radial orientation of the helix can be ensured. The helix gives rise to a photonic bandgap recognized as selective (Bragg) reflection of light[13,14] in a band $\Delta\lambda = p\Delta n$ around a central wavelength

$$\lambda_c = \overline{n}p\cos\theta \tag{1}$$

Here p is the helix period (pitch), $\Delta n = n_{\parallel} - n_{\perp}$ is the local birefringence (with $n_{\parallel}$ and $n_{\perp}$ the refractive indices along and perpendicular, respectively, to the local average molecule

Dr. Y. Geng, Dr. R. Kizhakidathazhath, Prof. J. P. F. Lagerwall
University of Luxembourg
Department of Physics and Materials Science
Luxembourg 1511, Luxembourg
E-mail: Jan.Lagerwall@lcsoftmatter.com
Dr. Y. Geng
School of Polymer Science and Engineering
Key Laboratory of Rubber-Plastics
Qingdao University of Science and Technology
Qingdao 266042, P. R. China
The ORCID identification number(s) for the author(s) of this article can be found under https://doi.org/10.1002/adfm.202100399.

DOI: 10.1002/adfm.202100399

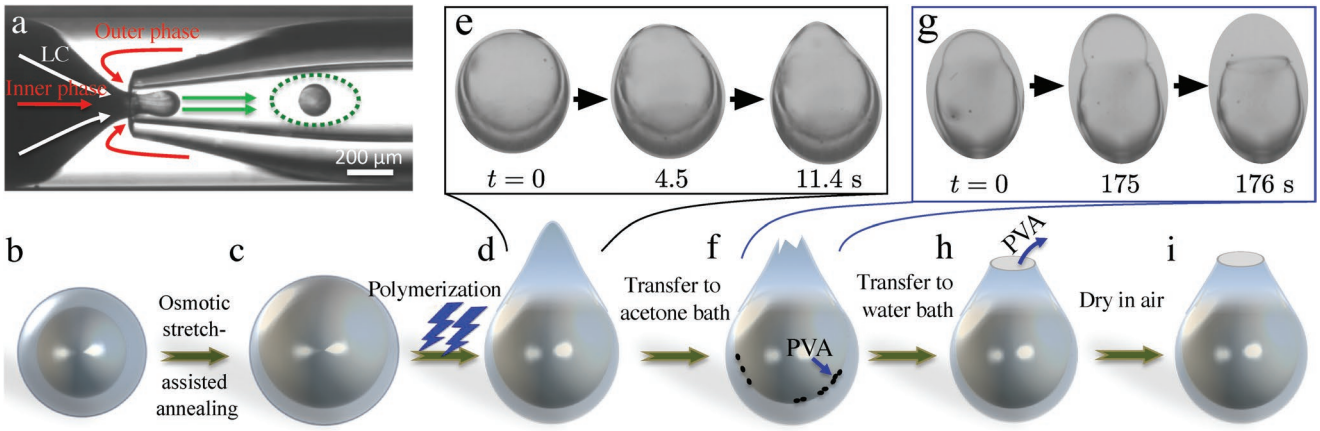

Figure 1. Overview of the process of making solidified, punctured, and residue-free CSR shells. a) Liquid-state reactive CLC shells are generated in a microfluidic set-up. The CLC is unaligned during shell production, scattering light, and thus appearing dark, blocking the view of the internal droplet. b,c) After production the shells are expanded and thinned by osmotic flow of water into the core, speeding up structural annealing. Buoyancy renders the shells thickest at the bottom and thinnest at the top. d) UV irradiation initiates solidification by polymerization, the resulting shrinkage causing a bulging-out near the thinnest point (snapshots from Video S1, Supporting Information (e); UV irradiation starts at t=0). f) The shells are transferred to an acetone bath during which the protrusion breaks off entirely or partially (snapshots from Video S2, Supporting Information (g)). h) Rinsing in water removes the PVA from the shell inside and i) drying in air yields empty punctured solid shells of high optical quality.

orientation), $\bar{n} = \sqrt{\frac{n_{\parallel}^2 + n_{\perp}^2}{2}}$ is the average refractive index experienced by light reflected by the helix[15] and θ is the angle of incidence with respect to the helix axis. The fundamental retroreflection corresponds to $\theta = 0$, at the maximum possible reflection wavelength, $\lambda_0 = \bar{n}p$.[11,16] Since p can be continuously tuned by varying the CLC mixture composition, λ_0 can easily be adjusted as desired, from UV to IR. Importantly, the reflected light is circularly polarized with the same handedness as the cholesteric helix.

The elucidation of the peculiar near-field optical properties of CSRs[16] and subsequent recognition that these properties turn CSR arrays into physical unclonable functions (PUFs),[17] of great value in anti-counterfeiting,[18] triggered a surge of follow-up research,[11,16,17,19–37] identifying many further application opportunities. In the present paper we instead target applications of the *far-field* selective retroreflection of CSRs, focusing on the ability to encode information unobtrusively onto surfaces. Using suitably designed CSRs, fiducial markers that humans will not notice can be distributed, allowing future human-populated environments to be as easy to navigate for robots as restricted environments are today.[11] To make the markers unnoticeable by the human eye, we must ensure—first—that any non-selective scattering is minimized. We solve this problem by realizing the CSRs as shells rather than droplets, and then polymerizing the CLC into a solid. The process opens up a small hole in every CSR, giving us access to the interior so we can remove all residues of stabilizers used in production and fill as well as surround the CSRs with a polymerizable liquid binder with optimized refractive index. Second, when designing markers operating in the IR regime, the effect of blue-shifted forward Bragg reflections must be taken into account in order to avoid unwanted visibility. Based on an analysis of how forward reflection is limited by refraction at the air–binder interface, and taking advantage of the internal retroreflection unique to CSR shells, we demonstrate that very good performance can be obtained.

2. Results and Discussion

2.1. Making Punctured Solidified CSR Shells that Do Not Scatter Light

CSR shells are born in the form of a thin layer of CLC, surrounding an inner droplet of immiscible isotropic liquid.[12] We achieve this configuration using a microfluidic pathway with nested glass capillaries,[38] as shown in **Figure 1**a. We have formulated two new optimized series of photopolymerizable CLC mixtures (full details of the chemistry and microfluidic procedure in the Section 4 and Supporting Information). One series uses a non-reactive chiral dopant (nrCD), allowing removal and recycling after polymerization, whereas the other (rCD) has 100% reactive components. For inner as well as outer phases we use an isotropic aqueous solution of polyvinylalcohol (PVA), providing interface stability and aligning the molecules tangentially to the interface, thereby promoting the desired radial helix orientation. Of great importance is the fact that the shells are asymmetric, with thin top and thick bottom (Figure 1c), due to density mismatch between the CLC (heavier) and the inner isotropic aqueous phase (lighter). The reverse asymmetry of opposite density mismatch would work equally well.

To speed up the annealing process after shell production, during which the CLC structure relaxes and adopts the radial helix orientation, the shells are placed in an outer phase with lower PVA content than that of the inner phase. This causes an osmotic flow of water into the inner aqueous droplet[39] (Figure 1b,c), increasing the shell radius and leading to an in-plane isotropic stretching of the shell.[40] This induces the same helix-orienting effect as "anisotropic deswelling," employed to align CLC elastomers[41,42] or suspensions of cellulose nanocrystals,[43,44] thereby assisting the stabilization of the radial helix configuration throughout the shell.

We initiate polymerization by shining UV light on the suspension (Figure 1d). In the self-closing spherical geometry of the shell, the shrinkage induced by polymerization of acrylate-based

reactive monomers[45] raises the internal pressure to a level where the thinnest point of the shell starts buckling outward to accommodate the incompressible aqueous inner phase, see Figure 1e and Video S1, Supporting Information. The pressure increase can be so great that the protrusion breaks off or ruptures, leaving a hole in the shell, but in most cases the shells end up deformed but intact at the end of polymerization.

The solid CSRs are now rinsed in pure water to remove all PVA residues from the outside, and then the aqueous continuous phase is replaced by acetone in order to remove any unreacted components (Figure 1f). The acetone swells the polymer and flows into the inner droplet. The highly deformed thin region around the protrusion cannot withstand the resulting strain, hence it ruptures, see Figure 1g and Video S2, Supporting Information. At the latest by the end of this stage, every shell thus has a single hole in the region where it is the thinnest.

The radial helical structure and characteristic CSR optical properties are preserved after polymerization and solvent rinse, with varying degree of color shift due to helix shrinkage for nrCD and rCD, respectively, also depending strongly on the chemical environment, see Figure S1, Supporting Information and related discussion. In **Figure 2** we show optical and electron microscopy images of polymerized shells that were dried directly from the acetone bath (Figure 1f) and from a second

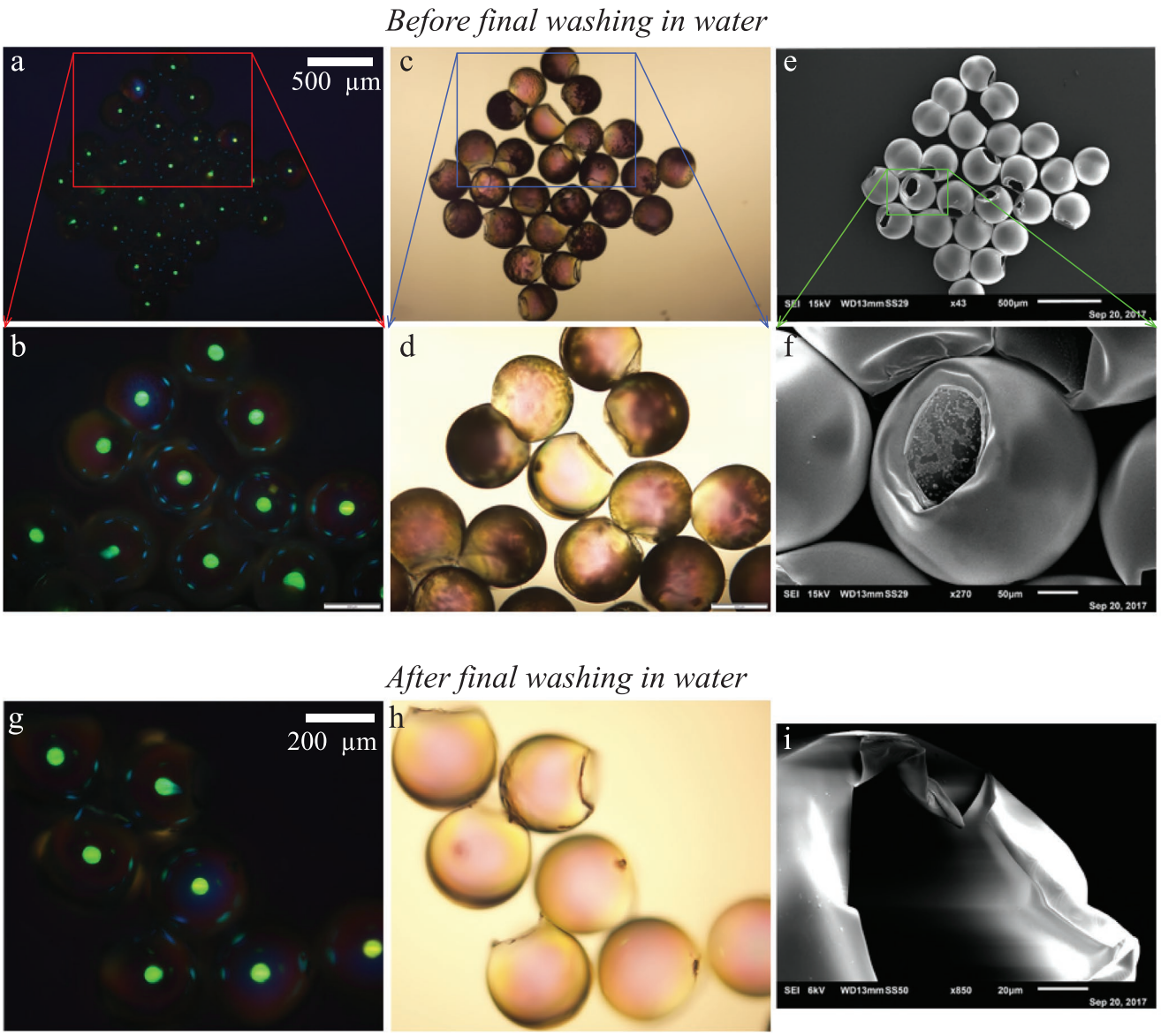

Figure 2. Optical and electron microscopy of polymerized and dried CSRs in air. The production follows Figure 1, in (a–f) without step Figure 1f. The CSRs in (g–i) went through also this final washing in pure water to remove internal PVA residues. Images (a), (b), and (g) are obtained by reflection POM (right-handed circular polarizer and analyzer) whereas (c), (d), and (h) are from transmission optical microscopy with linear polarizer but no analyzer. Images (e), (f), and (i) are obtained by scanning electron microscopy (SEM) on gold-coated CSRs. Panels (b), (d), and (f) are zoomed-in regions from (a), (c), and (e), respectively, as indicated by red, blue, and green lines.

water bath (Figure 1h), respectively. In the reflection polarizing optical microscopy (POM) photos we see that the optical quality remains excellent throughout the CSRs except in the direct vicinity of the hole, meaning that the puncturing has little negative impact on the overall CSR performance. However, viewing the shells dried from acetone in transmission (Figure 2c,d) we see dark shadows. These are due to PVA residue on the CSR insides, giving rise to significant scattering that renders the CSRs highly visible to the human eye, even in an optimized binder. PVA is insoluble in acetone, hence it precipitates on the CSR insides as a result of the first solvent exchange procedure, as easily seen in the zoomed-in SEM image in Figure 2f. This is the reason for the final water rinse, which removes also the internal PVA residue before the CSRs are dried in air (Figure 1e–g). After the rewashing, the CSRs are smooth on their insides as well as outsides (Figure 2i) and the transmission image no longer shows any shadows (Figure 2h).

2.2. Minimizing Visibility of IR-Reflecting CSRs via Optimized Binder: A Numerical Analysis

While it is easy to make the fundamental retroreflectivity invisible by tuning λ_0 to the UV or to the IR range, in actual usage, a CSR coating may be illuminated from any direction, and we may then experience forward Bragg reflections that are visible. As Equation (1) shows and as confirmed experimentally,[11] such forward reflections are blue-shifted compared to λ_0. If λ_0 is in the near-UV range, forward reflections are unimportant, as they arise further into the UV and are thus invisible. But for CSRs optimized for IR operation, for compatibility with standard night vision equipment, visible forward reflections can be a significant problem, see **Figure 3**a.

Fortunately, it is alleviated by the embedding of the CSRs in a binder, because the refraction at the air–binder interface limits the maximum incidence angle θ_m by which the light can reach the cholesteric helix (see Figure 3b–d), and thereby the magnitude of the blue shift. To quantify the effect and to formulate concrete design criteria, we carry out a basic numerical analysis within the simplifying constraints that all rays are in a single plane, passing through the centers of all CSRs considered. The full details are in the Sections S5–S7, Supporting Information. For CSRs embedded fully in a binder with refractive index n_b, we show in Section S7, Supporting Information that θ_m takes the value

$$\theta_m = 45^\circ + \frac{\arcsin(1/n_b)}{2} \tag{2}$$

The corresponding forward reflection path is not restricted to a single CSR, but it is mediated by cross communication between two adjacent CSRs, as illustrated in Figure 3b.

Equation (2) reveals that the maximum blue shift (as quantified by maximum θ_m) decreases with increasing n_b, hence for CSRs operating in the IR spectrum it is beneficial to work with high refractive index binders. However, any increase in n_b must maintain $n_b \approx \overline{n}$ to minimize scattering and specular reflection at the CSR–binder interfaces. To give some numerical examples of the range of blueshift, a practically convenient value $n_b = 1.5$ gives $\theta_m = 66°$, which reduces λ_c in Equation (1) by a factor of 0.41 compared to λ_0, corresponding to normal incidence ($\theta = 0°$). As we aim to prevent any reflections in the visible spectrum, corresponding to $0.4 < \lambda_c < 0.7$ μm, we should thus ensure $\lambda_0 = \overline{n}p \geq \frac{0.7}{0.41} = 1.7$ μm.

A retroreflection wavelength $\lambda_0 = 1.7$ μm is significantly longer than the operation range of standard night vision technology, the two regimes of which are 0.85 and 0.94 μm. However, because we use CSR shells as opposed to droplets, another interesting mode of retroreflection becomes available, namely that mediated by internal reflections,[24] shown experimentally in Figure 3e and illustrated with one example path in Figure 3f. This occurs at $\theta > 0$, hence with shells we can realize retroreflection visible to night vision cameras while maintaining $\lambda_0 \geq 1.7$ μm, thereby avoiding visible Bragg forward reflections if $n_b \geq 1.5$. For instance, the $m = 1$, $n = 3$ internal reflection path discussed in ref. [24] gives retroreflection from within the shell at $\theta = 60°$, corresponding to wavelengths $\lambda'_{60°} = 0.85$ μm for $\lambda'_0 = 1.7$ μm and $\lambda''_{60°} = 0.94$ μm for $\lambda''_0 = 1.88$ μm, thus optimum night vision reflectivity. Within the limitations of our simplified 2D analysis this would take place without visible reflections.

Also at identical illumination and observation directions, blue-shifted reflections arise by CSR cross communication,[16,17,29,32] see Figure 3g,h. This can give significant visibility even if $\lambda_0 > 700$ nm. However, these reflections occur at $\theta < \theta_m$, so if p is long enough to keep reflections at θ_m in the IR range, also the cross communication pattern will remain invisible.

To generalize the analysis, we also consider the forward reflection case of light incident from the left onto a vertical helix axis in a droplet CSR. We show nine such reflection paths in Figure 3c, with three different values of the incidence angle α and three different entry points defined by the distance L along the binder surface from the vertical central axis of the CSR. For simplicity, the refractive index of the binder is assumed to be perfectly adapted to the CSR, that is, the refractive index n_b of the binder is equal to the average CLC refractive index, $\overline{n}$; in the Supporting Information we additionally consider the cases with $n_b < \overline{n}$ and $n_b > \overline{n}$. In Figure 3d we show the corresponding Bragg reflection angles θ calculated as a function of α for $n_b < \overline{n}$, $n_b = \overline{n}$, and $n_b > \overline{n}$, respectively, with three different entry points (rescaled by the CSR radius R) and three different depths d (also rescaled by R). We see that θ decreases with increasing n_b, and that deeper embedding of the CSRs to greater depths d reduces θ for $n_b < \overline{n}$, while it increases θ if $n_b > \overline{n}$.

It is apparent from Figure 3a,c that a droplet is significantly worse than a shell in its undesired ability to produce blue-shifted forward reflections, thus potentially revealing CSRs designed for IR operation. This is because most reflections at high θ take place in the core of a droplet, where the corresponding shell has no CLC structure, hence such reflections are absent in CSR shells. Significantly, the inner part of a droplet gives no contribution to the desired retroreflectivity, which is saturated already by the first few microns around the perimeter.[17]

Summarizing the outcome of this numerical analysis, we can formulate the following design guidelines that should be taken into account when making CSR markers:

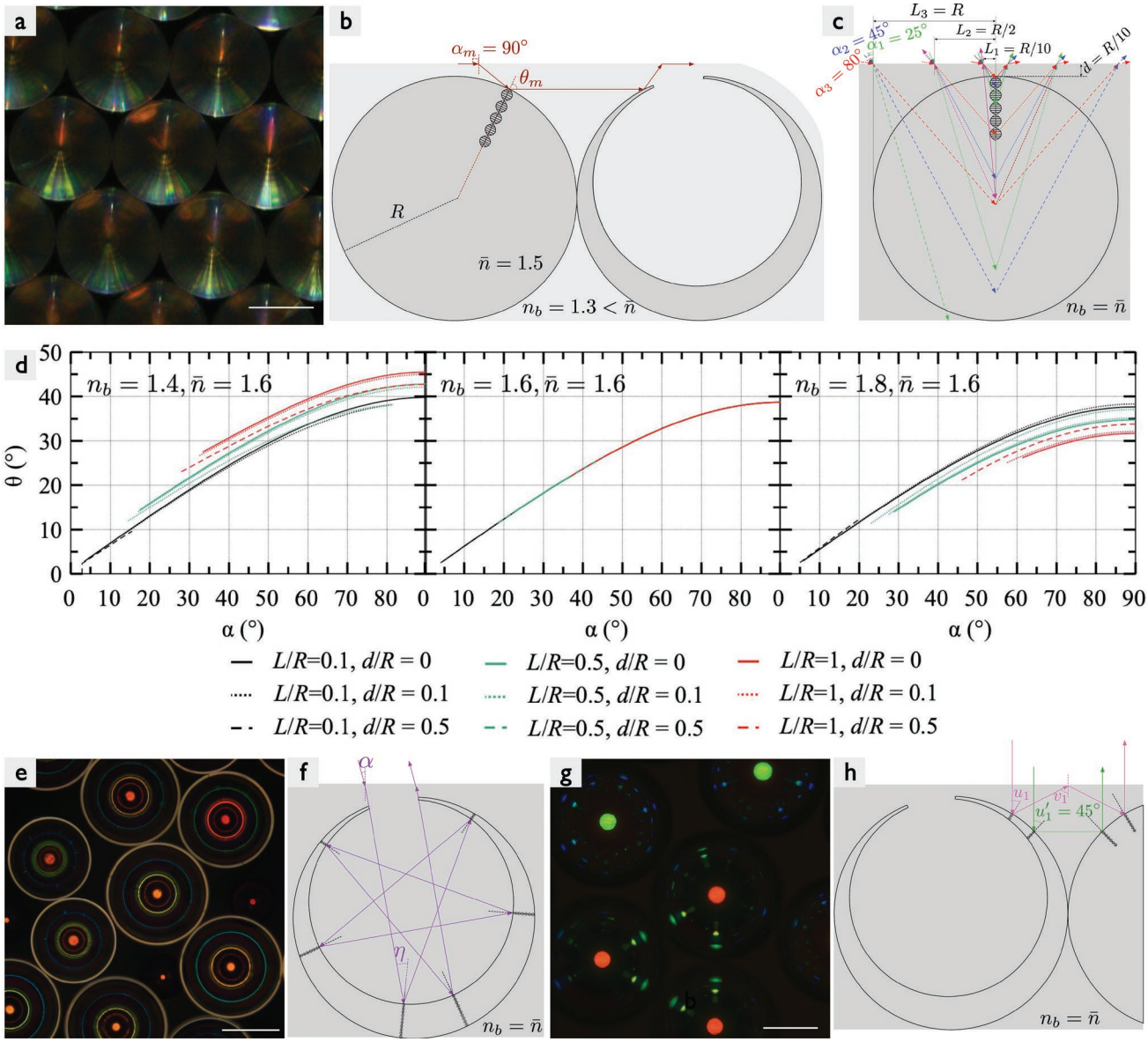

Figure 3. Impact on visibility of different CSR reflection modes. a) CSR droplets with $\lambda_0 \approx 1.5$ µm observed in reflection POM with diffuse illumination from the side. Although λ_0 is well into the IR, visible colors appear due to forward reflections. External forward reflection, giving the largest possible Bragg angle θ_m which corresponds to $\alpha_m = 90°$, is shown in (b) for $n_b = 1.3$. Internal reflections from the region with vertically oriented helix are illustrated in (c) for the case of index-optimized binder ($n_b = \bar{n} = 1.5$) at three different entry points L (dashed, dotted, continuous arrows) and three different incidence angles α (green, blue, red). Retroreflection is illustrated with pink double-headed arrows; no retroreflection is possible at L_3, which is too far from the CSR symmetry axis. The diagrams in (d) show all possible θ-values in the situation in (c), calculated as a function of α for $\bar{n} = 1.6$ and for three representative values each of n_b, d, and L. e,f) Retroreflection in shell CSRs can be mediated also by multiple internal reflections,[24] one example path of which is shown in (f). This gives rise to ring-like reflections at wavelengths shorter than λ_0, as seen in (e). g,h) Also the well-studied case of cross communication between adjacent CSRs illuminated and observed along the sample normal gives rise to reflections at wavelengths lower than λ_0.[16]

- The top of the CSRs should always be kept a non-zero depth d below the surface of the binder, in order to benefit from refraction at the air–binder interface to reduce the maximum effective CSR Bragg reflection angle θ_m, thereby minimizing the risk of visibility of IR-optimized CSRs.
- The refractive index n_b of the binder should be as high as possible to maximize the above effect (Equation (2)), but we must also ensure $n_b \approx \bar{n}$ in order to minimize scattering and specular reflection at the CSR–binder interface.
- Assuming that $n_b \geq \bar{n}$, the CSR should be as close to the binder–air interface as possible to minimize θ. Should $n_b < \bar{n}$, deeper embedding is instead preferable (Figure 3d).
- CSR shells are highly advantageous to droplets since: 1) shells enable internal retroreflection that provides retroreflectivity for night vision equipment while keeping the helix pitch p long enough to avoid visible Bragg reflections; and 2) shells limit Bragg reflections to the shell perimeter, thus removing many undesired high-θ reflections taking place near the center of CSR droplets.

2.3. Encoding Information with CSRs, and Extracting it with Polarized Photography

The binder serves the dual purpose of fixing the locations of the CSRs, such that they spell out machine-readable information, and to provide near index matching in order to minimize the risk that the human eye notices the CSRs. The hole in each CSR is now of utmost importance, as this allows an appropriately selected binder (the shared value $n_b \approx \overline{n}$ as high as possible) to fully embed the solidified CLC, on the outside as well as on the inside of the shell. It is imperative that the embedding is complete; any air bubbles lead to significant scattering. To this end, we dissolve the binder in acetone to ensure low viscosity before the CSRs are added. The acetone is gently evaporated and after ensuring that no air bubbles remain, and that all CSRs are in the right positions, the binder is cured into a solid by UV irradiation.

Given the anisotropy of the CLC structure it is impossible to achieve ideal index matching, but $n_b \approx \overline{n}$ is close enough to ensure very good results. In **Figure 4** we show coatings made by manually organizing CSR shells in the binder NOA160 ($n_b = 1.6$) into the letters ESMP and then UV-curing the binder to make the encoded information permanent. The CSRs are of rCD type with $\lambda_0 = 450$ nm (Figure 4a–f) and $\lambda_0 = 1.9$ µm (Figure 4g–l), respectively. The former are thus designed for deep blue reflection, giving no visible forward Bragg reflections, whereas the latter are tailored for shell-internal IR retroreflection and minimum visibility to the human eye. The coatings are placed on a dark and a bright background, respectively, for photography along a direction 45° to the coating normal, using regular room lighting as illumination in Figure 4a–b/g–h.

The $\lambda_0 = 450$ nm CSRs in Figure 4a–f are dark violet under ambient illumination, barely visible on the black background in Figure 4a. On the bright background of Figure 4b the letters are very near invisible. Note that the photos in Figure 4a,b,g,h have been taken very close up, in order to reveal any imperfections with maximum contrast. Consequently, significant scattering can be seen also from the background in Figure 4b/h, which to the naked eye appears uniformly white. In practice, the CSRs are thus even less visible than what these photos give the impression of. Interestingly, the shells are fully transparent in transmission microscopy (Figure 4c), in contrast to the long-pitch CSRs in Figure 4i. We attribute this to the helical modulation of the refractive index here being on such a short scale that light cannot resolve the variation, hence no scattering arises from the helix *per se*. Weak scattering can be seen along the CSR edges in panels Figure 4c,e, indicating that the NOA160—not tailored for the purpose—is not perfectly adapted to the CSRs.

Although visible light cannot resolve the variation in refractive index within the helix in these short-pitch CSRs, the system is of course still anisotropic. The effective optical anisotropy is seen in full when light travels perpendicular to the helix, with the minimum value $n_{min} = n_\perp$ for polarization along the helix and the maximum value $n_{max} = \sqrt{\frac{n_\parallel^2 + n_\perp^2}{2}} = \overline{n}$ for polarization perpendicular to it. In other words, for near-UV CSRs (here approximated by blue-reflecting CSRs), the average refractive index $\overline{n}$ in Equation (1) thus becomes equal to the maximum refractive index n_{max}, for visible light polarized perpendicular to the helix. We show in Section S8, Supporting Information, that also the relation between n_{max} and n_b is important: if $n_b < n_{max}$, total internal reflection (TIR) may occur between CSR and

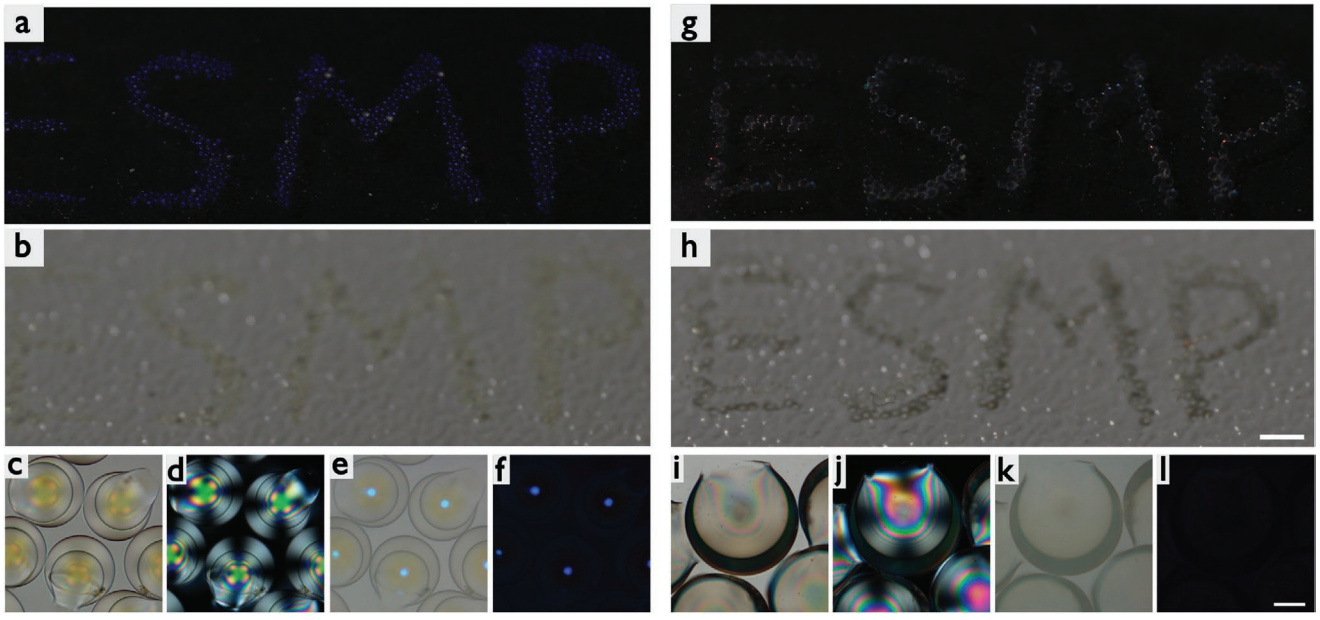

Figure 4. a–f) Coatings on glass slides in which the letters ESMP have been encoded using blue-reflecting and g–l) IR-reflecting CSR shells embedded in NOA160 binder. The binder provides near-optimum refractive index for the blue-reflecting CSRs, while the effective mismatch to the IR-reflecting CSRs is large enough to cause some visibility. The coatings are photographed at very close distance by a regular DSLR camera under ambient light on dark and bright backgrounds, respectively, in (a/g) and (b/h). Panels (c–f) and (i–l) show the two coatings in microscopy, in transmission without analyzer (c/i), transmission with crossed polarizers (d/j), reflection without analyzer (e/k) and reflection with right-handed polarizer and analyzer (f/l). Scale bar in (a–b/g–h) is 2 mm, in (c–f/i–l) 50 µm.

binder, which can trigger a waveguiding mode throughout the shell[24] that generates non-selective and unpolarized retroreflection, thus giving high visibility. For short-pitch CSRs, we can maintain the design guideline that $n_b \approx \overline{n}$, since $\overline{n} = n_{max}$, avoiding the risk of TIR while minimizing specular reflection and scattering.

As a consequence of their much longer p, significantly greater than visible light wavelengths, the CSRs with λ_0 = 1.9 µm are more visible in the highly exposing close-up photos in Figure 4g,h, in particular on the white background (Figure 4h). In the corresponding microscopy photos in panels i–l we see that the CSRs appear dark in transmission when viewing along the length of the shell, thus perpendicular to the helix. Light senses the periodic variation of refractive index along the helix axis in these long-p CSRs, causing scattering. In reflection microscopy without analyzer (k), more representative of how the coating will be seen during usage, the effect is much less prominent. Moreover, the bright background during microscopy overemphasizes the contrast compared to many cases of actual coatings, as any background other than white will make the CSRs less visible. We can conclude that CSR markers for IR operation are feasible for many but probably not all backgrounds, and not in contexts where even the slightest visibility is unacceptable; in such cases CSR markers for near-UV operation should be used. Compared to the results in Figure 4 some further improvement should still be expected by a fully optimized binder.

We demonstrate the ease in subtracting the background around a CSR coating using the λ_0 = 450 nm coating from Figure 4a–f placed in a regular room environment in **Figure 5**. The coating is illuminated by a white spotlight along the viewing direction. Panels in Figure 5a,b show the right- and left-handed polarized channels, respectively. Subtracting Figure 5b from Figure 5a we obtain nearly perfect background subtraction in Figure 5c, but the dark blue color is difficult to spot on the black background. By selecting only the blue channel and visualizing it in white, we finally get a very high-contrast image of the encoded information in Figure 5d, which is magnified in Figure 5e.

If p would be further reduced such that λ_0 = 400 nm, we can expect the CSRs to be practically invisible in an optimized binder, with equally effective background subtraction being possible as in Figure 5 using the band around λ = 400 nm. Unfortunately, standard circular polarizers, optimized for the middle of the visible spectrum, do not work well in this range, and standard cameras have a UV blocking filter that precludes imaging in the UV range. A modification of today's standard technology would thus be necessary to use such CSRs, but this is an exceptionally low-cost modification if done at the manufacturing stage: the only requirements are to refrain from fitting the blocking filter used in today's consumer-grade cameras and to make the λ/4-film of circular polarizers slightly thinner. A first demonstration of a simple fiducial marker with λ_0 = 400 nm illuminated by a near-UV ("blacklight") LED and imaged by a modified camera, in which the UV blocking filter has been removed, is shown and discussed in Section S9, Supporting Information.

We finally test the omnidirectional retroreflectivity of the CSR markers in the wavelength regimes for which they are designed, as well as their reflectivity in the visible spectrum when illumination and observation directions are different. In **Figure 6**, the two coatings of Figure 4 are photographed along different directions and with varying illumination directions. In rows Figure 6a,b, the photography and illumination directions are kept identical to test retroreflectivity (a small offset is unavoidable since the light source is always next to the camera

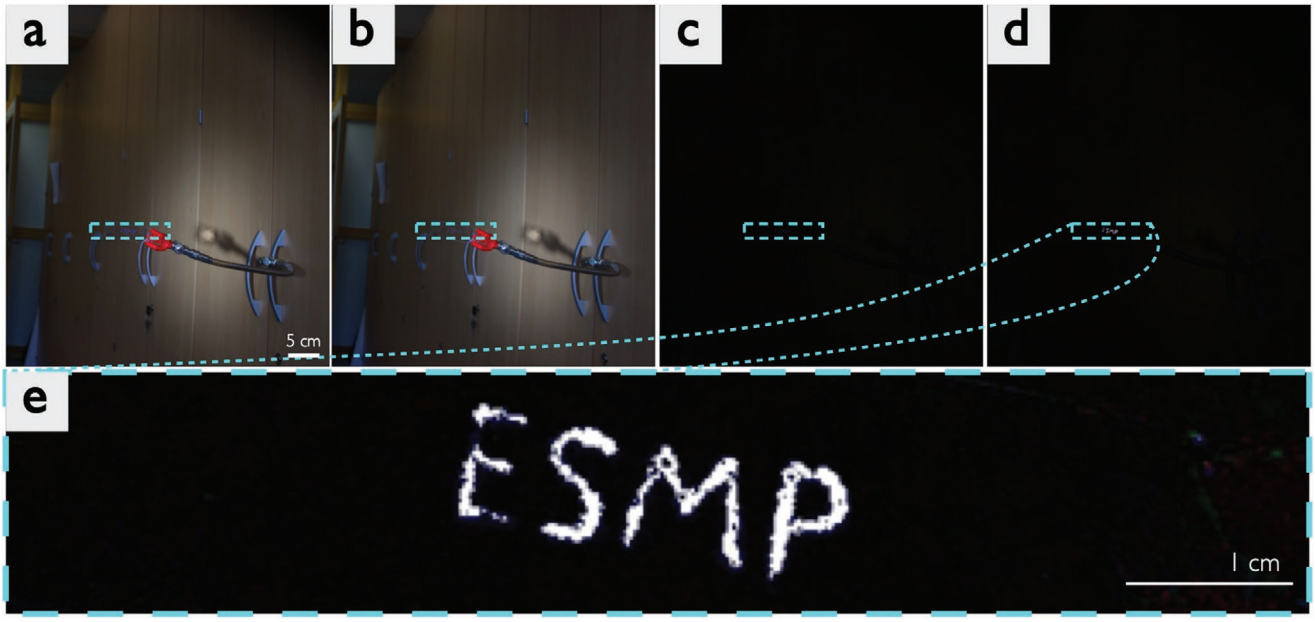

Figure 5. A coating with λ_0=450 nm CSRs spelling out four small letters is placed in a regular office environment and photographed through a) right and b) left-handed polarizer, respectively. The distracting background is removed very efficiently by subtracting (b) from (a), as shown in (c–e). In panel (d) the blue channel has been turned white for maximum contrast and in (e) the small letters are magnified in order to make them easy to read.

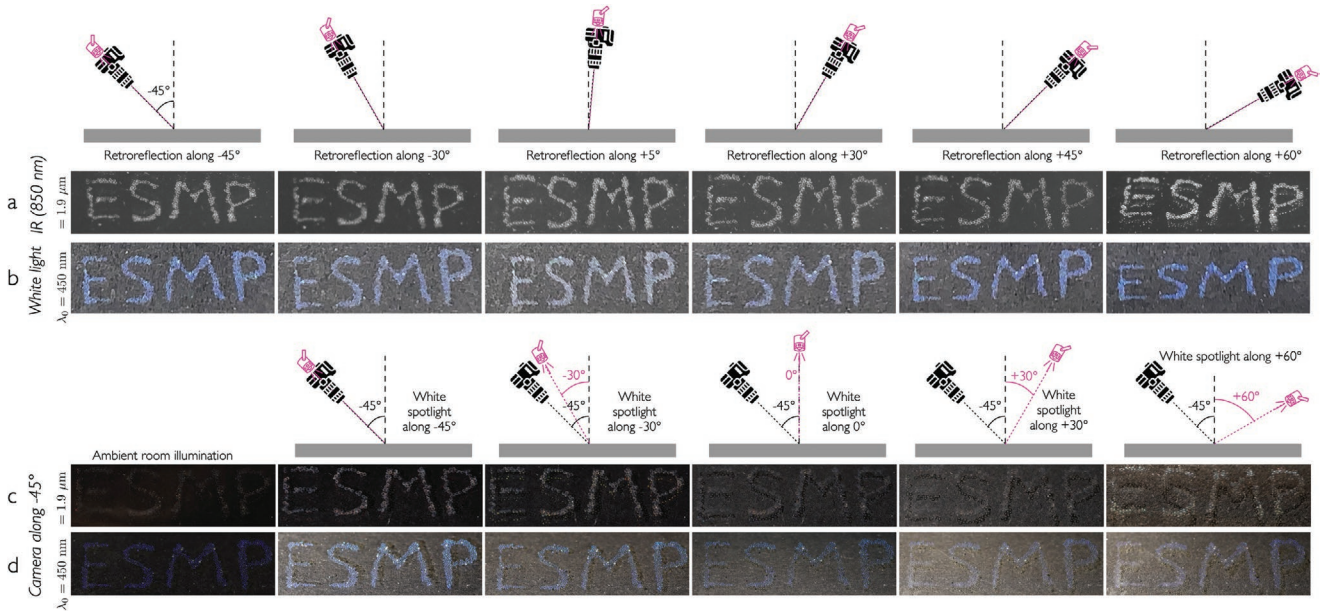

Figure 6. Assessing CSR reflectivity for varying illumination and viewing directions. a,b) Retroreflectivity along different directions for coatings optimized for IR retroreflection via shell-internal reflections (imaged using a modified camera with removed IR blocking layer, under 850 nm IR illumination only) and reflection at $\lambda_0 = 450$ nm, respectively. c,d) The same coatings imaged at −45° angle to the normal, under ambient light and for various directions of strong collimated white light illumination. The imaging and illumination geometries are illustrated above rows (a) and (c), respectively. The width of the encoded ESMP letters is 2.1 cm in (a/c) and 2.4 cm in (b/d).

objective), and we vary the angle with respect to the coating normal. Negative angles represent views from in front of the coating and positive angles from behind it, as illustrated in the cartoons above the photos. The row of photos in Figure 6a shows the $\lambda_0 = 1.9$ µm coating photographed using a modified DSLR camera in which the IR blocking film has been removed, with illumination by an IR LED operating at 0.85 µm wavelength (we obtained similar results, albeit at lower optical quality, also with a consumer grade night vision camera). No visible light was on during the experiments, hence to the operators the room appeared pitch black. The images clearly show omnidirectional retroreflectivity of the CSRs, thus confirming the shell-internal reflection at standard night vision IR wavelengths expected from the numerical analysis above. We tested the retroreflectivity with 0.85 µm as well as with 0.94 µm LEDs, obtaining very similar results. This is expected considering that there is a large range of internal reflection modes from CSR shells.[24]

Also the coating with $\lambda_0 = 450$ nm CSRs shows excellent retroreflective behavior, as seen in Figure 6b. The letters are clearly seen in blue irrespective of angle, somewhat diluted near normal incidence due to the non-selective (white) specular reflection from the coating–air interface superposing on the selective CSR reflections. This confirms that CSRs for $\lambda_0 = 400$ nm should be ideal for encoding information with omnidirectional readability for machines optimized for illumination and detection in this wavelength range, yet invisible to the human eye.

In Figure 6c,d we show the appearance of the two coatings as they are photographed at 45° angle to the normal under different illumination conditions. In the first column, the appearance under ambient light (regular ceiling lighting) is shown, confirming that both coatings are difficult to detect by the human eye under standard illumination conditions. In the remaining columns the two coatings are illuminated by a strong collimated white light source about 10 cm away, oriented along a range of directions as illustrated in the cartoons above row (Figure 6c). Such a photography and illumination setting seeks out the worst-case scenario in terms of keeping the CSRs hidden to humans. The $\lambda_0 = 1.9$ µm CSRs (Figure 6c) are clearly somewhat visible under these conditions, in particular when the light is from the same side of the coating as the camera but at a slightly different angle (column 3). Some points give a weak reddish reflection, and all CSRs show some specular reflection. In this photo we also see that light can be reflected to the viewer by the background after having been Bragg-reflected at large θ by the CSRs. The corresponding phenomenon under IR retroreflection conditions can be seen in the +60° photo on the far right of row (Figure 6a). Our coatings are mounted on microscope glass slides, elevating them from the background, which adds to the impact of such artifacts. These observations show that the 2D analysis in the section above needs to be refined to fully describe the optical behavior, considering also reflections from the background and probably also taking reflection paths extending out of the paper plane into account, to fully represent the complex 3D photonic behavior of CSRs.[29] Nevertheless, we see that already the design criteria that we could formulate based on our simplified analysis nearly take us to the target of invisible yet IR-retroreflective information-carrying coatings.

From an application point of view, it is important that the opening in each CSR does not impact the far-field reflection pattern. With a far-field illumination and imaging system used to localize the encoded information in a complex environment, the central as well as internal ring retroreflections are both visible, essentially regardless of how CSRs are oriented within the binder. Looking at the near-field cross communication

pattern in Figure S7n, Supporting Information, and comparing with the CSR contours, we note that the features are largely concentrated near the CSR insides, and the opening often does not prevent cross communication to take place. At the same time, both the relative locations of the central retroreflection spots and the overall communication pattern do depend on the orientation of the CSRs. Hence, in addition to allowing ideal embedding of CSRs in a binder, the polymerized and punctured CSRs add greatly to the unique PUF characteristics of CSRs that make them so powerful for secure authentication and anti-counterfeiting.[11,17,18]

3. Conclusion and Outlook

By developing a procedure for polymerizing cholesteric liquid crystal shells into solids with retained omnidirectional Bragg reflection, which opens a single small hole in each solidified shell that allows removal of all production material residues and internal and external embedding in a binder with optimized refractive index, we have demonstrated that the resulting cholesteric spherical reflector shells can be used to encode machine-readable information onto surfaces, while leaving them practically invisible to humans. This gives them enormous potential in opening the door to deploying fiducial markers for assisting robotic wayfinding in everyday environments, from cityscapes to offices to homes. Beyond providing landmarks for navigation, the circular polarization of CSR reflections makes the removal of the unpolarized background very easy, thus essentially eliminating the risk of false positives. Also augmented reality (AR) applications would benefit enormously by the invisible encoding of information in our environments.[11]

In particular when using short-pitch CSRs tailored for near-UV operation, we can expect that practically invisible fiducial markers can be realized by utilizing a fully optimized binder. The blue-shift of forward Bragg reflection renders it more challenging to design CSRs for IR night vision technology while ensuring invisibility to the human eye, but remarkably good results can be obtained by taking advantage of the refraction at the air–binder interface to limit the practical CSR forward reflection angle, in combination with the internal shell reflection to ensure retroreflectivity at night vision wavelengths. Our numerical analysis shows that CSRs should be fully embedded in the binder, but as close as possible to the surface, and that the refractive index n_b of the binder should be as high as possible, to minimize colorful reflections from CSRs optimized for IR operation. To minimize scattering and specular reflection at the binder–CSR interfaces, we must at the same time ensure $n_b \approx \overline{n}$, where $\overline{n}$ is the average refractive index of the CSRs. The analysis also shows that CSR shells are highly superior to droplets for applications in markers, hence the recently demonstrated method of making CLC shells using phase separation in droplets,[19] which can easily be scaled up to large-volume production of CSRs, may become very useful, as it is fully compatible with the new procedures presented in this paper.

An excellent first target where CSR-based fiducial markers could be introduced is construction, which at present is in the process of being increasingly automized using robots, hence the markers could be included in building components as the environment is being constructed. To make on-road autonomous vehicles safer, it would also be highly beneficial to deploy CSR-based fiducial markers on other road occupants, at least on newly produced vehicles, later also on existing ones. Bicyclists could have the markers on helmets. With time, human-occupied surroundings would thus gradually become much easier to navigate for autonomous vehicles and other mobile robots, without any impact for human occupants since the markers are invisible to them. This would bring us significantly closer to a stage where the presence of robots in human-populated environments poses no added risk of accidents.

4. Experimental Section

To prepare the solidified CLC shells, mixtures of different liquid crystalline reactive monomers (RMs) and chiral dopants (CDs) were first carefully formulated (details in the Supporting Information). All the RMs and CDs used were acquired from Synthon GmbH, Germany, and used as received. As photoinitiator, 4 wt% (in the whole mixture) of IRGACURE 819 (Ciba, Switzerland) was added, also used as received. Each mixture was stirred for 2 h, the vial immersed in a water bath at around 80 °C to facilitate mixing.

All shells were produced in nested glass capillary microfluidic devices (details in the Supporting Information), following the basic principle of Utada et al.[38] The CLC mixture was flowed as middle phase through the voids between an outer square capillary and an inner cylindrical injection capillary. The outer phase (a 5 wt% isotropic aqueous solution of PVA) was flowed from the other side in the opposite direction in the voids between the same square capillary and an inner cylindrical collection capillary. The inner phase (10 wt% PVA aqueous solution) was flown through the injection capillary in the same direction as the CLC mixture. When the immiscible phases met close to the two cylindrical capillary orifices, flow focusing of the LC, with encapsulated inner phase, into the outer phase resulted if all three flow speeds were optimized, see Figure 1a. The microfluidic set-up was mounted in a heating stage set to 32 °C for ensuring that the CLC was in the liquid crystalline state during the production. The shells were then annealed at 32 °C inside an incubator (dark) for 7 days until the helix was uniformly radial-aligned, without the oily streak defects typical of an unaligned cholesteric phase.

A UVATA LED UV curing system (delivering 8800 mW cm^{-2} at full power) was used to initiate the polymerization process. After polymerization, the solvent exchange processes using first acetone and then water took place in order to remove the non-reactive CD and the remaining PVA which deposited on the shell inner surface during the acetone washing process (details in the Supporting Information). The shells were then dried and mixed with binders NOA81, NOA160, and NOA170 (Norland Products Incorporated, US), with refractive indices 1.56, 1.6, and 1.7, respectively, to prepare coatings. First, shells were dispersed into a mixture of NOA and acetone (1:1 in volume), left standing still in a closed environment for around 12 h in order to let the binder diffuse into the core of each shell. Second, the acetone was evaporated in a fumehood for around 12 h, and then the suspension of shells in binder was transferred onto a glass slide. During this process, shells were arranged in a certain pattern or kept naturally random, as desired. Polymerization of the binder was initiated by shining UV light, which rendered the final coatings.

The shells were investigated in a polarizing microscope (Olympus BX51, Japan) equipped with a digital camera (Olympus DP73, Japan). For macroscopic and far-field photography a Canon EOS 77D (Japan) was used in the visible range, whereas for photography in the UV and IR ranges a modified Canon 7D MK II was used in which the IR- and UV-blocking filters had been removed (modification by LDP LLC, USA), illuminating the sample with a UV-LED (Onforu BlackLight Spotlight, 30 W, $\lambda = 385 - 400$ nm) or IR-LED (Wilktop 60° 10 W Night Vision LED, $\lambda = 850$ nm), respectively. SEM imaging was done using a JEOL JSM-6010LA (Akishima, Japan), operated in 12–15 kV range using an

in-lens secondary electron detector. For SEM imaging, samples were gold coated (around 5 nm thickness) using a Quorum Q150R ES coater (Quorum Technologies Ltd, Laughton, East Sussex, England).

Supporting Information

Supporting Information is available from the Wiley Online Library or from the author.

Acknowledgements

Financial support from the European Research Council (ERC, Proof of Concept project VALIDATE, grant code 862315), National Natural Science Foundation of China (NSFC) (No. 51403095), and the Office of Naval Research Global (project LAB'RINTH) is gratefully acknowledged. The authors are grateful to Z. Tosheva and M. Melchiorre for assistance with sample preparation for SEM, and to M. Schwartz for valuable discussions.

Conflict of Interest

The authors declare no conflict of interest.

Data Availability Statement

The data that support the findings of this study are openly available in OSF at https://osf.io/hwprc/?view_only=8a683451305c40efb501fa083f522ac0.

Keywords

cholesteric spherical reflector, information encoding, liquid crystals, omnidirectional bragg reflection, polymerization-induced deformation, refractive index matching

Received: January 14, 2021
Revised: February 18, 2021
Published online: March 18, 2021

[1] H. Igliński, M. Babiak, *Proc. Eng.* **2017**, *192*, 353.
[2] J. Kim, M. Schwartz, A. Zarzycki, *Complexity and Simplicity - Proc. of the 34th eCAADe Conf., eCAADe, Brussels, Oulu* **2016**, *1*, 53.
[3] A. L. Alfeo, E. C. Ferrer, Y. L. Carrillo, A. Grignard, L. A. Pastor, D. T. Sleeper, M. G. Cimino, B. Lepri, G. Vaglini, K. Larson, M. Dorigo, A. Pentland, in *2019 Int. Conf. on Robotics and Automation (ICRA)*, IEEE, Piscataway, NJ **2019**, pp. 4233–4240.
[4] S. Jones, E. Milner, M. Sooriyabandara, S. Hauert, *Adv. Intell. Syst.* **2020**, *2*, 2000110.
[5] U. Z. A. Hamid, Y. Saito, H. Zamzuri, M. A. A. Rahman, P. Raksincharoensak, *Int. J. Veh. Auton. Syst.* **2018**, *14*, 134.
[6] M. Klomp, M. Jonasson, L. Laine, L. Henderson, E. Regolin, S. Schumi, *Veh. Syst. Dyn.* **2019**, *57*, 1028.
[7] L. Zhang, W. Xiao, Z. Zhang, D. Meng, *IEEE Access* **2020**, *8*, 209356.
[8] J. Wei, J. M. Snider, J. Kim, J. M. Dolan, R. Rajkumar, B. Litkouhi, *2013 IEEE Intelligent Vehicles Symp.*, IEEE, Piscataway, NJ **2013**, 763.
[9] Y. Li, Y. Zheng, B. Morys, S. Pan, J. Wang, K. Li, *IEEE Intell. Transp. Syst. Mag.* **2020**, https://doi.org/10.1109/MITS.2019.2907633.
[10] A. Sagitov, K. Shabalina, L. Sabirova, H. Li, E. Magid, *Proc. of the 14th Int. Conf. on Informatics in Control, Automation, and Robotics*, ICINCO, Madrid, Spain **2017**, *2*, 182.
[11] M. Schwartz, G. Lenzini, Y. Geng, P. B. Rønne, P. Y. Ryan, J. P. Lagerwall, *Adv. Mater.* **2018**, *30*, 1707382.
[12] M. Urbanski, C. G. Reyes, J. Noh, A. Sharma, Y. Geng, V. S. R. Jampani, J. P. Lagerwall, *J. Phys.: Condens. Matter* **2017**, *29*, 133003.
[13] H. Kitzerow, C. Bahr, *Chirality in Liquid Crystals (Partially Ordered Systems)*, Springer, Berlin **2000**.
[14] F. Castles, S. Morris, in *Handbook of Liquid Crystals* (Eds: J. W. Goodby, P. J. Collings, T. Kato, C. Tschierske, H. Gleeson, P. Raynes), Vol. *3*, Wiley-VCH, Weinheim, Germany **2014**, 493–520.
[15] E. Priestley, in *Introduction to Liquid Crystals* (Ed: E. Priestley), Springer, Berlin **1975**, 203–218.
[16] J. Noh, H.-L. Liang, I. Drevensek-Olenik, J. P. Lagerwall, *J. Mater. Chem. C* **2014**, *2*, 806.
[17] Y. Geng, J. Noh, I. Drevensek-Olenik, R. Rupp, G. Lenzini, J. P. Lagerwall, *Sci. Rep.* **2016**, *6*, 26840.
[18] R. Arppe, T. J. Sørensen, *Nat. Rev. Chem.* **2017**, *1*, 0031.
[19] S. Park, S. Lee, S. Kim, *Adv. Mater.* **2020**, *32*, 2002166.
[20] A. Belmonte, M. Pilz da Cunha, K. Nickmans, A. P. H. J. Schenning, *Adv. Opt. Mater.* **2020**, *8*, 2000054.
[21] A. Belmonte, T. Bus, D. J. Broer, A. P. Schenning, *ACS Appl. Mater. Interfaces* **2019**, *11*, 14376.
[22] D.-B. Myung, S.-Y. Park, *ACS Appl. Mater. Interfaces* **2019**, *11*, 20350.
[23] S. Lee, J. Kim, Y. Kim, S. Kim, *Sci. Adv.* **2018**, *4*, eaat8276.
[24] Y. Geng, J.-H. Jang, K.-G. Noh, J. Noh, J. P. Lagerwall, S.-Y. Park, *Adv. Opt. Mater.* **2018**, *6*, 1700923.
[25] H. J. Seo, S. S. Lee, J. Noh, J.-W. Ka, J. C. Won, C. Park, S.-H. Kim, Y. H. Kim, *J. Mater. Chem. C* **2017**, *5*, 7567.
[26] S. S. Lee, H. J. Seo, Y. H. Kim, S.-H. Kim, *Adv. Mater.* **2017**, *29*, 1606894.
[27] K. Noh, S. Park, *Mater. Horiz.* **2017**, *4*, 633.
[28] J.-H. Jang, S.-Y. Park, *Sens. Actuators, B* **2017**, *241*, 636.
[29] Y. Geng, J. Noh, I. Drevensek-Olenik, R. Rupp, J. Lagerwall, *Liq. Cryst.* **2017**, *44*, 1948.
[30] Y. Li, J. Jun-Yan Suen, E. Prince, E. Larin, A. Klinkova, H. Thérien-Aubin, S. Zhu, B. Yang, A. Helmy, O. Lavrentovich, E. Kumacheva, *Nat. Commun.* **2016**, *7*, 12520.
[31] H.-G. Lee, S. Munir, S.-Y. Park, *ACS Appl. Mater. Interfaces* **2016**, *8*, 26407.
[32] J. Fan, Y. Li, H. K. Bisoyi, R. S. Zola, D.-k. Yang, T. J. Bunning, D. A. Weitz, Q. Li, *Angew. Chem., Int. Ed.* **2015**, *54*, 2160.
[33] S. J. Aβhoff, S. Sukas, T. Yamaguchi, C. A. Hommersom, S. Le Gac, N. Katsonis, *Sci. Rep.* **2015**, *5*, 14183.
[34] S. S. Lee, B. Kim, S. K. Kim, J. C. Won, Y. H. Kim, S.-H. Kim, *Adv. Mater.* **2015**, *27*, 627.
[35] S. S. Lee, S. K. Kim, J. C. Won, Y. H. Kim, S.-H. Kim, *Angew. Chem., Int. Ed.* **2015**, *54*, 15266.
[36] E. Beltran-Gracia, O. Parri, *J. Mater. Chem. C* **2015**, *3*, 11335.
[37] Y. Uchida, Y. Takanishi, J. Yamamoto, *Adv. Mater.* **2013**, *25*, 3234.
[38] A. Utada, E. Lorenceau, D. Link, P. Kaplan, H. A. Stone, D. Weitz, *Science* **2005**, *308*, 537.
[39] T. Lopez-Leon, V. Koning, K. B. S. Devaiah, V. Vitelli, A. Fernandez-Nieves, *Nat. Phys.* **2011**, *7*, 391.
[40] V. S. R. Jampani, R. H. Volpe, K. Reguengo de Sousa, J. Ferreira Machado, C. M. Yakacki, J. P. F. Lagerwall, *Sci. Adv.* **2019**, *5*, eaaw2476.
[41] S. T. Kim, H. Finkelmann, *Macromol. Rapid Commun.* **2001**, *22*, 429.
[42] R. Kizhakidathazhath, Y. Geng, V. S. R. Jampani, C. Charni, A. Sharma, J. P. F. Lagerwall, *Adv. Funct. Mater.* **2020**, *30*, 1909537.
[43] C. Schütz, J. R. Bruckner, C. Honorato-Rios, Z. Tosheva, M. Anyfantakis, J. P. F. Lagerwall, *Crystals* **2020**, *10*, 199.
[44] B. Frka-Petesic, G. Kamita, G. Guidetti, S. Vignolini, *Phys. Rev. Mater.* **2019**, *3*, 045601.
[45] D. Broer, J. Lub, G. Mol, *Nature* **1995**, *378*, 467.